Ambient Stable and Efficient Monolithic Tandem Perovskite/PbS Quantum Dots Solar Cells via Surface Passivation and Light Management Strategies

Citation: Tavakoli, M. M., Dastjerdi, H. T., Yadav, P., Prochowicz, D., Si, H., Tavakoli, R., Ambient Stable and Efficient Monolithic Tandem Perovskite/PbS Quantum Dots Solar Cells via Surface Passivation and Light Management Strategies. Adv. Funct. Mater. 2021, 31, 2010623.

As Published: http://dx.doi.org/10.1002/adfm.202010623

Publisher: Wiley

Persistent URL: https://hdl.handle.net/1721.1/140297

Version: Author's final manuscript: final author's manuscript post peer review, without publisher's formatting or copy editing

Ambient Stable and Efficient Monolithic Tandem Perovskite/PbS QDs Solar Cells via Surface Passivation and Light Management Strategies

Mohammad Mahdi Tavakoli,[1,2‡] Hadi Tavakoli Dastjerdi,[3‡] Pankaj Yadav,[4] Daniel Prochowicz,[5] Huayan Si,[6] Rouhollah Tavakoli[2]*

[1]*Department of Electrical Engineering and Computer Science, Massachusetts Institute of Technology, Cambridge, 02139 MA, USA*

[2]*Department of Materials Science and Engineering, Sharif University of Technology, 14588 Tehran, Iran*

[3]*Department of Materials Science and Engineering, Massachusetts Institute of Technology, Cambridge, 02139 MA, USA*

[4]*Department of Solar Energy, School of Technology, Pandit Deendayal Petroleum University, Gandhinagar-382 007, Gujarat, India*

[5]*Institute of Physical Chemistry, Polish Academy of Sciences, Kasprzaka 44/52, 01-224 Warsaw, Poland*

[6]*School of Materials Science and Engineering, Hebei Provincial Key Laboratory of Traffic Engineering materials, Shijiazhuang Tiedao University, Shijiazhuang 050043, P. R. China*

‡ These authors contributed equally to this work.

* Corresponding author: mtavakol@mit.edu

Abstract

Although highest tandem efficiencies have been reported for the perovskite/silicon and perovskite/perovskite configurations, they suffer from poor stability of the low-bandgap tin-based perovskite subcell. Thus, finding new low-bandgap materials with good stability is

This is the author manuscript accepted for publication and has undergone full peer review but has not been through the copyediting, typesetting, pagination and proofreading process, which may lead to differences between this version and the Version of Record. Please cite this article as doi: 10.1002/adfm.202010623.

required for the fabrication of stable and all solution-processed monolithic (two-terminal (2T)) tandem solar cells. Among all tandem configurations, a 2T tandem device composed of an organometallic perovskite (high bandgap) and PbS colloidal quantum dots (QDs) (low bandgap) absorbers by considering the perovskite device as a front cell would be so interesting owing to the excellent air-stability of the PbS QDs. In fact, fabrication of PbS QDs (low bandgap) on top of perovskite cells (high bandgap) is problematic due to the fabrication issues and there is not any successful report for this configuration**.** Therefore, mostly researchers reported a simple mechanically attached perovskite and PbS QDs subcells (i.e., four-terminal (4T)) tandem device. Here, we reported highly efficient and stable monolithic (2T) perovskite/PbS QDs tandem solar cells, where the perovskite solar cell (PSC) acts as the front cell and the PbS QDs with a narrow band gap acts as the back cell. Specifically, we employed ZnO nanowires (NWs) passivated by SnO_2 as an electron transporting layer (ETL) for PSC front cell, leading to a single cell PSC with maximum power conversion efficiency (PCE) of 22.15%, which is the most efficient NWs-based PSCs in the literature. By surface passivation of PbS QDs by $CdCl_2$, we achieved QDs devices with improved V_{OC} and a PCE of 8.46% (bandgap of 0.92 eV). After Proper optimization, two- and four-terminal tandem devices with stabilized PCEs of 17.1% and 21.1% were achieved, respectively, where our 2T tandem device shows the highest efficiency reported in the literature for this design. Since in the front cell, we replaced spiro HTL with a stable hole transporting layer (CuPC), our 2T tandem cell shows excellent operational stability over 500 h under continuous illumination with only 6% PCE loss. More importantly, the tandem design without any packaging depicts impressive ambient stability (almost no change) after 70 days in an environment with controlled 65% relative humidity (RH), thanks to the superior air stability of the PbS QDs.

Introduction

Low-cost processing and promising optoelectronics properties of organic-inorganic perovskite materials with ABX_3 crystal structure (A: Methylammonium (MA), Formamidinium (FA), Cesium (Cs); B: Pb, Sn; X: I, Br, Cl) make them ideal candidates for the fabrication of high efficiency and stable thin film solar cells.[1-4] Over the past years, extensive efforts in terms of compositional engineering, interface engineering, additive engineering and surface passivation have been devoted to improving the efficiency and stability of the perovskite solar cells (PSCs).[5-10] This results in a certified power conversion efficiency (PCE) of 25.5% for single junction device, which is very close to the Shockley-Queisser limit.[11] In order to improve the efficiency and stability of the PSCs, many research groups modified the electron transporting layer/perovskite interfaces,[12,13] developed new perovskite compositions with improved crystallinity and absorption,[14-16] and passivated the surface of perovskite films using different modulators such as chlorine additives[17,18] and two-dimensional (2D) perovskites.[19-21] Basically, single junction solar cells suffer from two inevitable energy losses i.e., the transmittance of photons with low energy and thermalization of photons with high energy. These losses greatly limit the efficiency of the device and can be addressed using a tandem design.[22] In order to further push the efficiency of the PSCs above the Shockley-Queisser limit, it is highly desirable to develop tandem devices by combination of PSCs with other semiconductor solar cells such as silicon cells, which have a great potential to absorb in the infrared region. Lin et al.[23] modified the composition of low-bandgap Pb-Sn perovskite using metallic tin powder to control the oxidation of Sn^{2+} to Sn^{4+} and fabricated a 2-T perovskite/perovskite tandem solar cell with PCE of over 24.8%. Recently, Xu et al.[24] fabricated 2T perovskite/silicon tandem device with impressive PCE up to 27% by proper modification of the large bandgap perovskite back cell composition using

triple-halide alloys. Even though perovskite/silicon and perovskite/perovskite tandem devices shows impressive efficiency, they suffer from poor stability of the low bandgap perovskite subcell due to the poor stability of the tin-based perovskite film.[8] Therefore, finding new and air-stable active layers with absorption in near- and mid- infrared range of the solar spectrum for the back call is crucial.

Among the infrared absorbing materials, PbS quantum dots (QDs) appear as an attractive alternative for silicon due to the ease of fabrication, low-cost processing, and bandgap tunability and for perovskite due to excellent air-stability.[25-30] In fact, by controlling the size of PbS QDs, the bandgap can be easily tuned to efficiently absorb the light in the infrared range.[31,32] Recently, Sun et al.[33] reported PbS QDs solar cell with a certified PCE of 13.8% by reducing the interdot spacing using a monolayer of perovskite film. However, the combination of low-bandgap PbS QDs and high-bandgap perovskite absorbers in a tandem configuration has been rarely investigated. In fact, fabrication of monolithic (2T) perovskite/PbS QDs tandem devices is challenging due to all technical issues during the processing. For example, the solvents such as acetonitrile can dissolve the perovskite film and therefore, Zhang et al.[22] considered the use of PbS QDs as a front cell and perovskite layer as a back cell in their tandem configuration. They reported a 2T tandem cell with a PCE of 11%, however, the proposed cell architecture increases the energy loss due to considering the PbS QDs as a front cell. The recent theoretical study by Karani et al.[34] revealed that tandem device with an ideal PCE of 43% can be achieved using perovskite absorber with a bandgap of 1.55 eV (front cell) and PbS QDs with a bandgap of 1 eV (back cell). Thus, extensive efforts over time are required to achieve such high PCE for perovskite/PbS QDs device.

Since fabrication of 2T tandem devices is a big challenge, most of the researchers prefer to simply fabricate 4T tandem solar cells by mechanically attachment of both subcells. In this regard, Manekkathodi *et al*.[35] reported 4T perovskite/PbS QDs tandem device by fabrication of semitransparent PSCs using MoO_3/Au/Ag/MoO_3 top electrode and mechanically attachment of two subcells, which resulted in PCE of 20.2%. Later, Chen *et al*.[36] improved the design of perovskite/PbS QDs 4T tandem device and achieved a PCE of 24%.

In this study, we fabricated an efficient and stable monolithic (2T) perovskite/PbS QDs tandem device by considering the perovskite (large bandgap) as front cells and the PbS QDs (small bandgap) as back cells. We first improved the efficiency and stability of each subcell using light management strategy (NWs-based device) and interface engineering (ZnO NWs/SnO_2) for the PSC front cells and surface passivation of PbS QDs for the back cells. Based on these modifications, we achieved high PCEs of 22.15% for the NWs-based PSC and 8.46% for the Cd-doped PbS QDs device with great stability. Finally, based on proper optimization, two- and four-terminal perovskite/PbS QDs tandem devices with stabilized PCEs of 17.1% and 21.1% were achieved, respectively, where the 2T device shows the highest reported PCE in the literature. Notably, the main advantage of our tandem device is its stability. Our monolithic tandem device shows excellent operational stability under continuous illumination for more than 500 h with only 6% PCE loss. Regarding ambient stability, the results are more promising since the PbS QDs has a great air stability. The 2T tandem device maintained its initial PCE value after 70 days in an environment with 65% RH, whereas the single junction PSC lost almost 37% of its initial efficiency in the same condition. Our novel tandem design (perovskite/PbS QDs) with descent efficiency addresses the poor stability of perovskite/perovskite and silicon/perovskite tandem devices thanks to the air-stability of the PbS QDs. Overall, our achievements in this study open up a new class of

solution-based tandem solar cells, which has a great potential for the commercialization purpose without using any packaging.

Results and Discussions

ZnO nanowire-based perovskite solar cells:

While ZnO NWs are widely used as an ETL for the fabrication of efficient organic and PbS QDs solar cells, there is a comparatively limited attention in their use in PSCs due to often encountered chemical instability of ZnO/perovskite interface.[37,38] In this study, we deposit double-A cation perovskite (methylammonium (MA)/ formamidinium (FA)) on ZnO NWs ETL grown by hydrothermal technique (Figure S1). Figures 1a and 1b show the scanning electron microscopy (SEM) images of the decomposed perovskite film annealed on top of ZnO NWs with different magnifications. As seen, there are three different regions in the film containing only PbI_2 flakes, perovskite crystals, and mixed PbI_2 and perovskite phases. UV-visible spectrum (Figure 1c) and x-ray diffraction pattern (XRD) (Figure 1d) indicate the presence of PbI_2 phase in the perovskite film, which is in good agreement with the SEM images.[39] Notably, we may have some δ phase after annealing in the perovskite film. There are two approaches to tackle with this stability issue i.e. annealing of perovskite film at low temperature (70 °C) or applying an interface layer between ZnO NWs and perovskite.

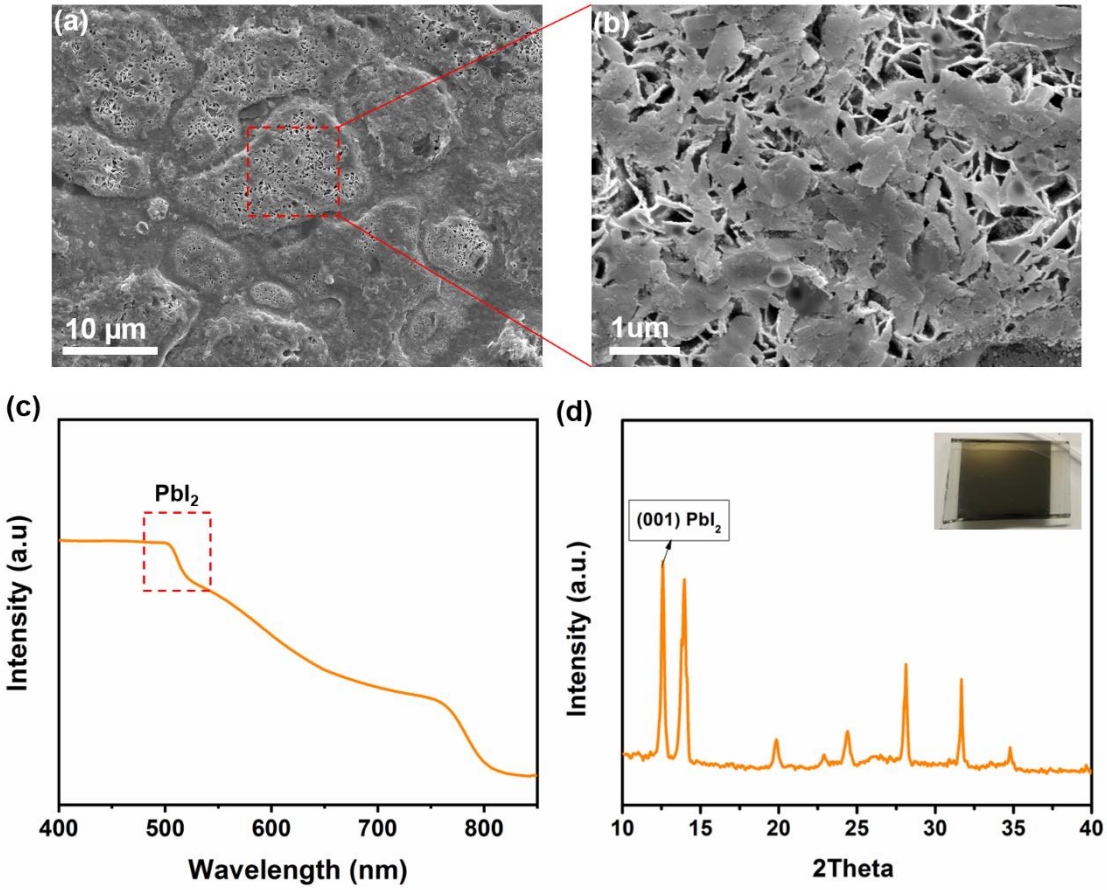

Figure 1. **Perovskite reaction with ZnO NWs during the annealing process**. Top view SEM images of perovskite film annealed on top of ZnO ETL at 100 °C for 5 min with low (a) and high (b) magnifications. (c) UV-visible spectrum and (d) XRD pattern of the corresponding perovskite film on ZnO ETL, indicating the presence of PbI_2 phase. The inset image in Figure 1D is the photograph of perovskite film annealed on ZnO NWs array.

In this context, we passivate the surface of ZnO NWs with a thin layer of amorphous SnO_2 (4 nm), deposited by atomic layer deposition (ALD). Figure 2a-c shows the schematic of device fabrication on the ZnO NWs/SnO_2 ETL. As seen, the ZnO NWs were grown on the ITO glass coated by a ZnO seed layer (Figure 2a). Then, a conformal layer of SnO_2 was deposited on the ZnO NWs array using ALD method (Figure 2b). Transmission electron microscopy (TEM) images shown in Figure S2 confirms the presence of uniform amorphous SnO_2 layer

around the ZnO NW with an interplanar d-spacing of 0.26 nm (corresponded to the (002) planes).[39] We also measured the photoluminescence spectra of the NWs and NWs/SnO_2 samples and observed a near band emission peak located at ~380 nm and a broader green emission peak (defect peak) at the visible region for both samples (Figure S3). The enhanced PL peak at 380 nm and the quenched green emission peak for the NWs/SnO_2 sample clearly shows that the SnO_2 layer passivates the surface defects of the NWs array,[12] which is also consistent with the X-ray photoelectron spectroscopy (XPS) results (Figure S4, Supplementary Note 2). The XPS results indicate that ALD deposition of SnO_2 on the surface of ZnO NWs array can passivate the surface defects of NWs and reduce the presence of oxygen vacancies and especially hydroxyl groups, resulting in high quality ZnO NWs array.[40]

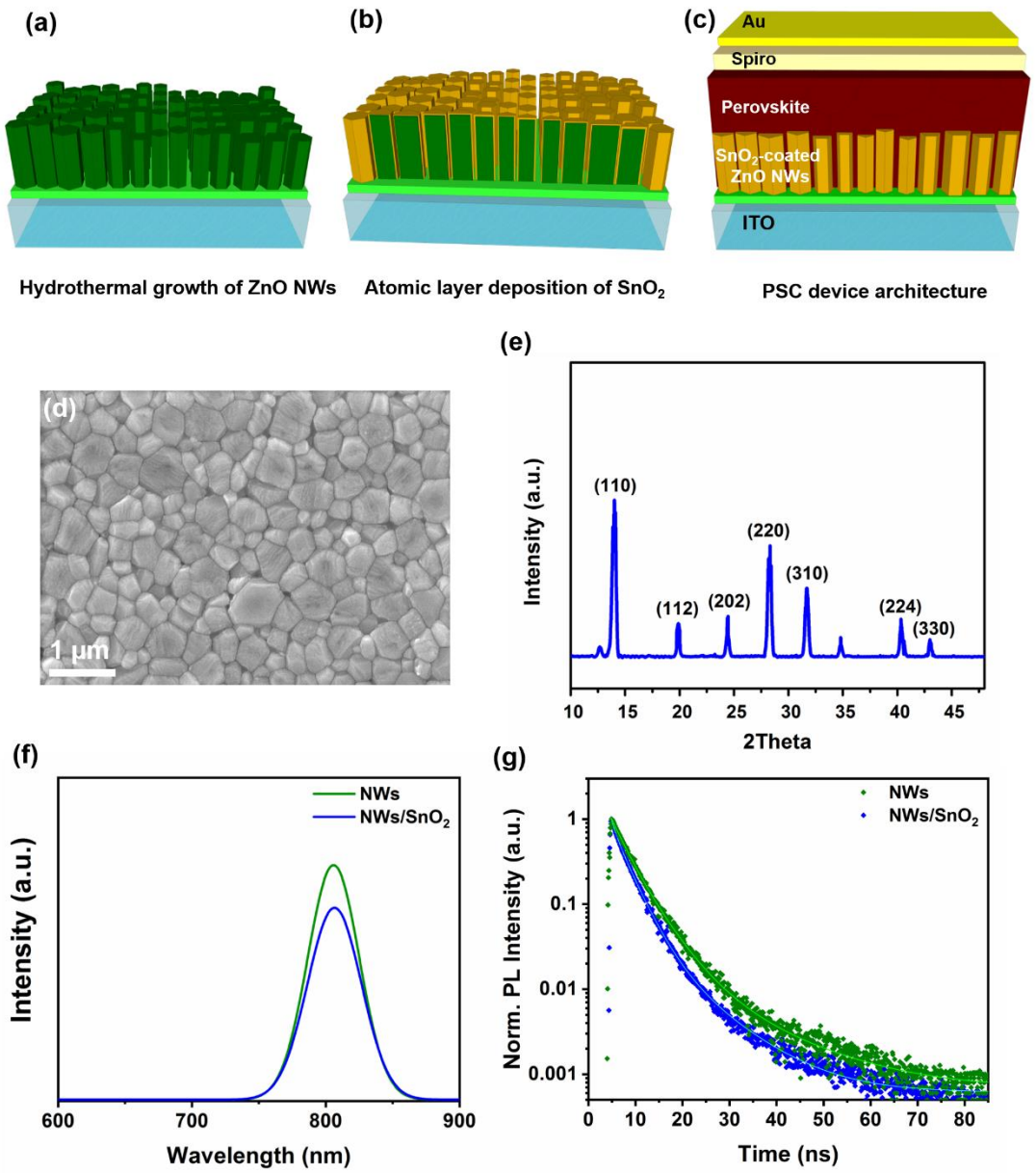

Figure 2. **Film characterizations of NWs and NWs/SnO_2 ETLs**. Schematics of device fabrication steps. (a) Hydrothermal growth of ZnO NWs, (b) Atomic layer deposition of SnO_2, and (c) schematic of device architecture. (d) Top-view SEM image and (e) x-ray diffraction pattern of the perovskite film deposited on ZnO NWs/SnO_2 ETL. (f) Photoluminescence spectra and time-resolved photoluminescence curves (g) of the perovskite films deposited on ZnO NWs with and without SnO_2 layer.

Figure 2d shows SEM image of the perovskite film deposited on the NWs/SnO_2 ETL (annealed at 150 °C), indicating a pinhole-free morphology and great crystallinity of the perovskite film. Moreover, the perovskite film has an average grain size of ~420 nm, as confirmed by atomic force microscopy (AFM) analysis as well. As shown in Figure S5, the perovskite film has a smooth surface with a roughness of 23±5 nm. XRD pattern of the perovskite film, shown in Figure 2e, indicates excellent crystallinity of the perovskite film with a small peak of PbI_2, originated from excess PbI_2 in the perovskite composition. In order to study the effect NWs array on optical properties, we have measured the transmittance spectra of the ZnO NWs/ITO glass, and SnO_2/ZnO NWs/ITO glass samples as compared to the ITO glass and planar ZnO/ITO glass, as shown in Figure S6a. NWs array generally causes optical scattering, which results in a longer optical path length in the absorber layer and increases the probability of the optical absorption in the perovskite film.[41,42] As seen in Figure S6a, the NWs based sample has 6-10% more transmittance over the entire wavelengths as compared to the planar sample, indicating their effect on light trapping properties. This can drastically enhance the perovskite absorption and thus increase the current density in the device. Figure S6b depicts UV-visible spectra of the perovskite films on NWs and NWs/SnO_2 ETLs indicating similar bandgap of ~1.55 eV and higher absorption of perovskite film on NWs/SnO_2 sample due to its better crystallinity. Steady-state photoluminescence (PL) spectroscopy reveals that perovskite film on NWs/SnO_2 sample has stronger quenching effect as compared to the NWs sample (Figure 2f). Thus, a better charge transfer at the interface of perovskite/NWs/SnO_2 is expected as compared with the perovskite/ZnO. When we have a stronger quenching effect, it means that the electrons can quickly transfer from the perovskite layer to the ETL before they recombine with holes. For the case of ZnO/SnO_2/perovskite sample, the electrons transfer from perovskite to the ETL faster than the ZnO/perovskite one. Therefore, in ZnO/SnO_2/perovskite case, the chance of

non-radiative recombination is lower than the ZnO/perovskite sample and we have a better charge transfer.[10,12] We also performed time-resolved PL (TRPL) spectroscopy for the corresponding samples, as shown in Figure 2g. Biexponential model was used to fit these data as summarized in Table S1. The perovskite film on NWs/SnO_2 ETL shows shorter lifetime than the perovskite on pure NWs, which is in good agreement with the PL results. In addition to the above results, we also compared the optical properties of perovskite films deposited on planar ZnO/SnO_2 and ZnO NWs/SnO_2 ETLs, as illustrated in Figure S7. We find that the NWs-based sample shows higher absorption due to better light trapping properties of NWs and stronger quenching effect due to larger surface area as compared to the planar sample.[5]

To study the influence of the SnO_2 interface layer on the device performance, PSCs based on NWs and NWs/SnO_2 ETLs were fabricated. Figure 3a shows the cross-sectional SEM image of NWs/SnO_2-based PSC with the following architecture: ITO/ZnO NWs/SnO_2 coated-ZnO NWs/perovskite/spiro-OMeTAD/gold.

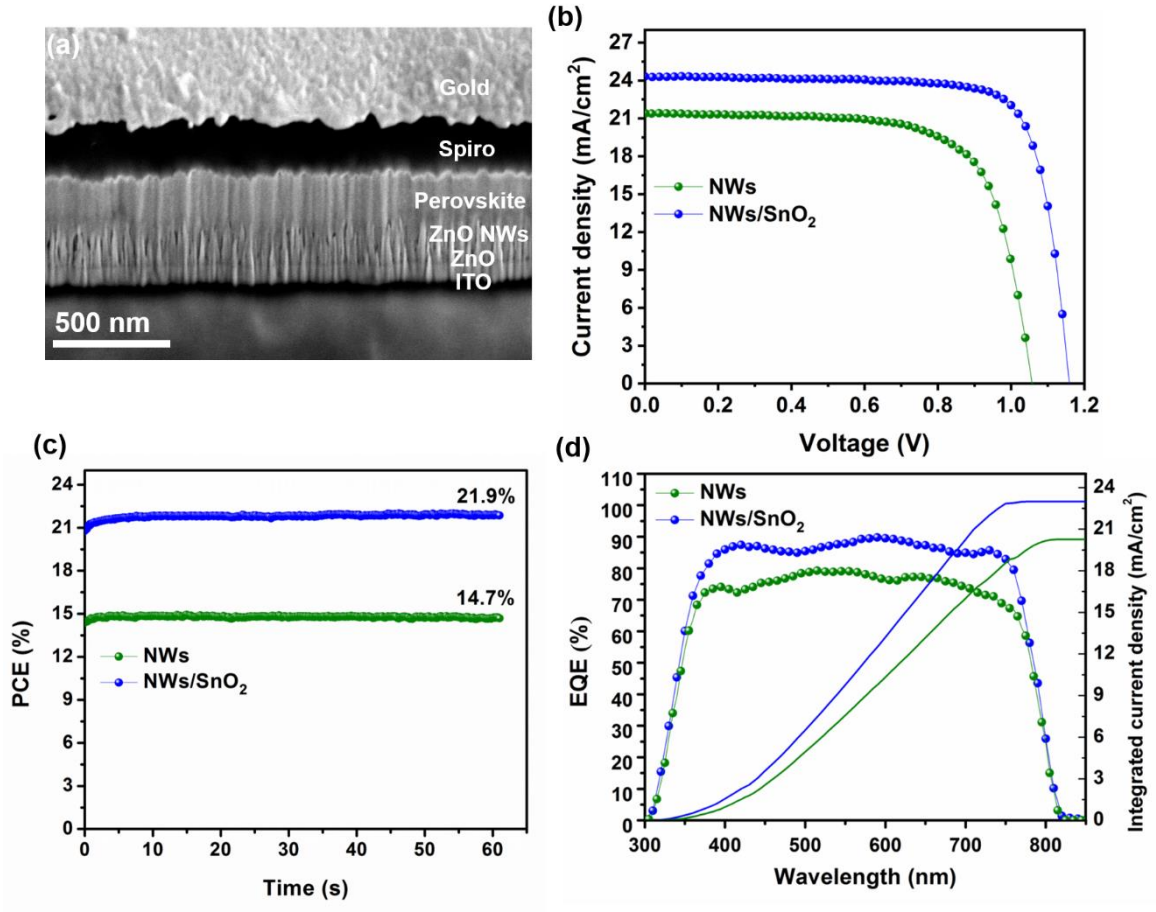

Figure 3. Photovoltaic characterizations of PSCs fabricated on ZnO NWs and ZnO NWs/SnO_2 ETLs. (a) Cross-sectional SEM image of PSC based on NWs/SnO_2 ETL, taken by focused ion beam milling (FIB) SEM. (b) J-V curves, (c) maximum power point tracking, and (d) EQE spectra of PSCs fabricated on ZnO NWs and ZnO NWs/SnO_2 ETLs.

The current density-voltage (J-V) curves of the best performing PSCs fabricated on the NWs and NWs/SnO_2 ETLs are shown in Figure 3b, which are measured under standard AM1.5G condition and reverse scan. The photovoltaic (PV) parameters of the corresponding PSCs are listed in Table S2. The champion PSC with ZnO NWs ETL shows a V_{OC} of 1.05 V, a J_{SC} of 21.3 mA/cm^2, a fill factor (FF) of 67%, and a decent PCE of 15%. The main reason of poor efficiency is due the use of low temperature (70 °C) for annealing of the perovskite film, which could control the deteriorate reaction between perovskite and ZnO NWs but also leads

to the formation of poor-quality perovskite films with point defects/low crystallinity. In contrast, the NWs/SnO_2 based device indicates improved V_{oc} of 1.16 V, high J_{sc} of 24.4 mA/cm^2, and FF of 78%, resulting in a maximum PCE of 22.15%. As seen, using surface passivation of NWs array by SnO_2, the V_{OC} and FF are improved relatively by 10% and 16%, respectively. We confirmed our PCE results by measuring the maximum power point (MPP) of the corresponding devices, as shown in Figure 3c. From these results, the PSCs on NWs and NWs/SnO_2 ETLs indicate stabilized PCE of 14.7% and 21.9%, respectively. Notably, the optimum average length of NWs array is around 200 nm and by increasing the NWs length, the PCE is dropped possibly due to the shunting effect or higher series resistance in the device (Figure S8). We also compared the J-V results of the PSCs fabricated on ZnO and ZnO/SnO_2 planar ETLs, as shown in Figure S9. Similarly, the ZnO/SnO_2 planar device shows a high PCE of 19.38%, which is much better than the ZnO planar PSC (11.85%). The NWs/SnO_2 based PSC shows the highest efficiency due to better light absorption (J_{sc}) as than that of ZnO/SnO_2 planar device. In fact, using the NWs array, the J_{SC} and PCE of the PSCs are enhanced relatively by 12% and 14.3%, respectively, due to the light trapping effect. To validate the values of J_{sc} of the representative PSCs, external quantum efficiency (EQE) was measured as shown in Figure 3d. After integration of EQE results with the solar spectrum, J_{sc} of 20.2 mA/cm^2 for NWs device and 23.1 mA/cm^2 for the NWs/SnO_2 device were obtained, which are in good agreement with the corresponding J-V results. In order to evaluate the V_{oc} enhancement in the NWs/SnO_2 device, electrochemical impedance spectroscopy (EIS) was performed as shown in Figure S10. We found that the NWs/SnO_2 device shows lower series resistance (R_s) and larger recombination resistance (R_{Rec}) as compared to the NWs PSCs, which can explain the observed higher FF and V_{OC} in the NWs/SnO_2 device, respectively. Additionally, we performed ultraviolet photoelectron spectroscopy (UPS) measurements for the NWs and NWs/SnO_2 ETLs and found that the band offset between the conduction band

of perovskite film and the NWs/SnO_2 ETL is less than that of NWs ETL, resulting in a better electron transfer at the interface of perovskite/ETL (Figure S11). Figure S12 depicts the statistics of PV parameters for the PSCs fabricated on NWs and NWs/SnO_2 ETLs. As seen, the average values of PV parameters for the NWs/SnO_2 PSCs are higher than those of the ZnO NWs ones, which indicate the same trend as the best performing devices. We also measured the average values of hysteresis indices (HIs) for NWs and NWs/SnO_2 based PSCs as illustrated in Figure S13. We find that the average value of HI for the NWs/SnO_2 based PSCs (1.09%) is lower than that of (1.46%) the NWs devices, which can be correlated to the stronger quenching effect in the device with NWs/SnO_2 ETL. Besides, the operational stability of the PSCs on NWs and NWs/SnO_2 ETLs was monitored over 200 h under continuous illumination and nitrogen environment (Figure S14). Interestingly, the NWs/SnO_2 device retains 92% of its initial PCE after 200 h, whereas the NWs cell degrades quickly, possibly due to the light activated chemical reaction at the ETL/perovskite interface.

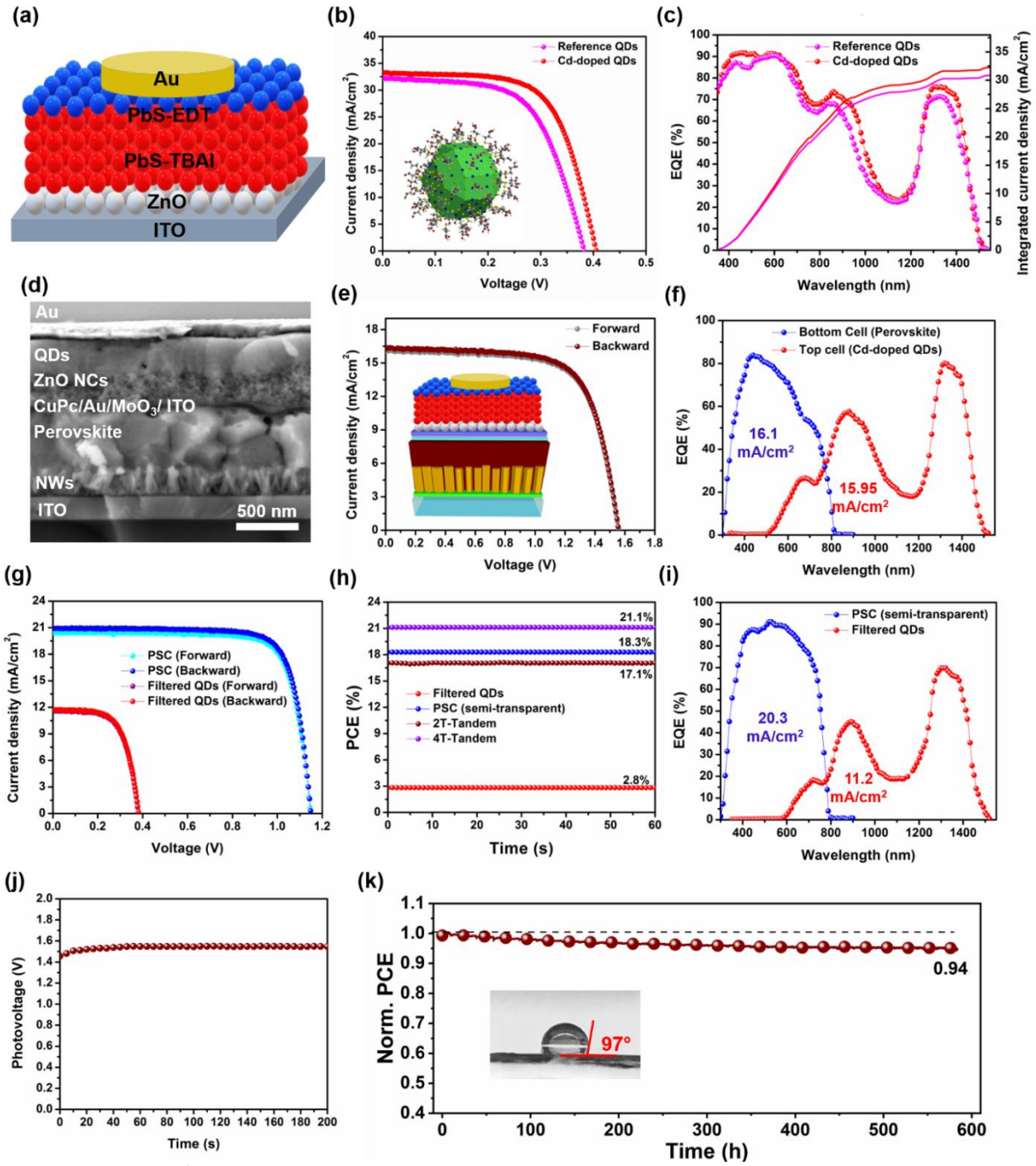

Figure 4. **Device characterization of QDs and Tandem solar cells**. (a) Schematic of device architecture for PbS QDs solar cells. (b) J-V curves (The inset image indicates a single quantum dot passivated by Cd atoms and TBAI ligands) and (c) EQE spectra of PbS QDs solar cells without and with Cd doping. (d) Cross-sectional SEM image of 2T-tandem perovskite/PbS QDs solar cell. (e) J-V curves of 2T-tandem perovskite/PbS QDs solar cell

with forward and backward scan directions. The inset image shows the schematic of device structure. (f) EQE curves of back and front subcells in 2T-tandem design. (g) J-V curves of semi-transparent PSC and PbS QDs device filtered by semitransparent PSC. (h) Maximum power point tracking of the 2T-tandem perovskite/PbS QDs, semi-transparent PSC, filtered PbS QDs, and 4T-tandem perovskite/PbS QDs devices. (i) EQE spectra of semi-transparent PSC, filtered PbS QDs, and tandem perovskite/PbS QDs devices in 4T tandem design. (j) Stabilized photovoltage over 200 s and (k) operational stability test of 2T-tandem perovskite/PbS QDs device under illumination and nitrogen flow for 580 h.

PbS QDs solar cells:

PbS QDs semiconductors are excellent active layers for absorbing photons in near- and mid-infrared ranges of a solar spectrum.[22] To evaluate the potential of PbS QDs semiconductors, we synthesized a set of QDs with bandgap of 0.92 eV, 1.12 eV, and 1.3 eV by controlling their QDs sizes (Figure S15) and studied their effect on the PV performance of PbS QDs devices as explained in the Supporting Information. To further increase the V_{oc} of the low-bandgap PbS QDs, we reduced the surface defects of PbS QDs by atomic passivation technique. For this purpose, $CdCl_2$ with low electron affinity was employed to passivate the surface of PbS QDs.[43] Figure S17 shows the XPS spectra of the QDs without and with $CdCl_2$ doping, supporting the presence of both Cd (406.4 eV) and Cl (199.6 eV) atoms on the surface of the PbS QDs. TRPL spectra of the PbS QDs (bandgap of 0.92 eV) before and after Cd doping shown in Figure S16, indicate longer lifetime for the Cd-doped PbS QDs. Figure 4a shows the schematic of PbS QDs device demonstrating an architecture of ITO/ZnO/TBAI-capped PbS QDs/EDT-capped PbS QDs/Au. J-V curves of the PbS QDs devices without and with Cd passivation are shown in Figure 4b. Table S4 shows the PV parameters of the corresponding devices. As seen, all photovoltaic parameters are improved drastically, due to

reduction of the surface defects of PbS QDs through Cd passivation. The PCE and especially V_{oc} of the PbS QDs (Bandgap of 0.92 eV) device are increased from 7.32% and 0.38 V for reference to 8.46% and 0.41 V for Cd-doped device, respectively. The V_{oc} enhancement (7.8%) caused by Cd passivation is further confirmed by EIS measurement as shown in Figure S18, indicating lower R_s and higher R_{Rec} in the Cd-doped QDs device compared with the reference cell. Additionally, upon Cd passivation the current density of PbS QDs device is increased as proved by EQE measurement. The EQE results show that the PbS QDs devices yield in a high EQE (over 50%) in the ranges of 800-1000 nm and 1200-1400 nm. After integration of EQE spectra by the solar spectrum, J_{SC} values of 30.8 and 32.2 mA/cm^2 were achieved for the reference and Cd-doped PbS QDs devices, respectively, which are in good agreement with J-V results. We further investigated this enhancement by UPS measurement and found that the Cd-doped PbS QDs has smaller band offset with respect to the ZnO ETL as compared to that of the reference QDs (Figure S). Figure S20 shows the J-V curves of Cd-doped PbS QDs solar cells fabricated using different size of the QDs. Table S5 depicts the average PV parameters of the corresponding devices. As seen, by decrease in the bandgap of the PbS QDs, the J_{SC} of the device significantly increases due to improved absorption in the infrared range, however, the V_{OC} drops because of lower bandgap of the QDs. Therefore, there is a trade-off between J_{SC} and $V_{OC.}$ Although the PCE of the PbS QDs devices is dropped by decrease of the bandgap, the current match between top and bottom solar cells in a tandem configuration is a key parameter and need to be improved for further increase in the PCE of tandem devices. For this purpose, PbS QDs layer with higher absorption in the infrared range are required.[34] One of the main advantages of QDs devices is their excellent stability in ambient conditions, where the PCE of the devices remains invariant after 150 days (Figure S21). This could be beneficial for improving the stability of the PSC devices in a monolithic tandem device architecture using the QDs device as a back cell.

Perovskite/PbS QDs tandem devices:

In order to fabricate perovskite/PbS QDs tandem devices, we fabricated semi-transparent PSCs using ITO glass as top electrode and copper (II) phthalocyanine (CuPC) as HTL. After proper optimization, we fabricated semi-transparent PSCs as front cells in a 2T-tandem design by changing the HTL and top electrode of front cells. In particular, we employed CuPC and Au (1 nm)/MoO_3/sputtered ITO as HTL and recombination layer, respectively, and optimized the device performance and the thickness of perovskite active layer, in order to match the current density in both subcells. In fact, spiro HTL due to having some dopants and high optimum thickness reduces the stability of the tandem device and increases the parasitic absorption. Since CuPC is a stable HTL, does not require any dopant and can be deposited uniformly with low thickness by thermal evaporation, it would be a great replacement for the spiro HTL.[44] As reported in the literature,[45] Au (1 nm) gold nanocluster is an excellent recombination layer, which improves the FF and V_{OC} of the tandem device. Moreover, the purpose of the MoO_3 thin layer is band alignment and protection of the underneath layers from the damages caused by ITO sputtering.[45] We used different thicknesses of perovskite layer in 2T and 4T tandem devices by changing the concentration of solution in order to improve the efficiency. Figure 4d shows the cross-sectional SEM image of a 2T-tandem perovskite/PbS QDs device, which is consisted of ITO/ZnO/ZnO NWs/SnO_2/Perovskite/CuPC/Au/MoO_3/sputtered ITO/ZnO NCs/PbS QDs/Au. The J-V curves of the best performing 2T-tandem device measured under forward and reverse scan directions are shown in Figure 4e. Interestingly, our 2T-tandem device shows a high V_{oc} of 1.55 eV, a relatively high J_{sc} of 16.3 mA/cm^2, a FF of 69%, resulting in a high PCE of 17.43% under reverse bias (Table S6). In fact, the device depicts almost the same trend under forward scan with slightly lower PCE of 16.96%. Figure S22 demonstrates the J-V curves of

2T-tandem devices fabricated by QDs with different sizes. The average PV parameters of each device are listed in Table S7. Here, we have optimized the thickness of the perovskite films with respect to the QDs size and the optimum values were summarized into the Table S7. The thickness of the perovskite film was optimized for each QDs size in order to increase the current match in both subcells. The optimum thickness of perovskite films was 240 nm, 360 nm, and 450nm for QDs (950 nm), QDs (1100 nm), and QDs (1350 nm), respectively. As seen, by decrease the bandgap of the QDs, the current match in the tandem device is increased significantly due to the higher absorption in the infrared range, which is the main reason of obtaining high PCE of 17.1% for the monolithic tandem device using QDs with bandgap of 0.92 eV. In order to study the current match in our optimized 2T-tandem device, EQE test was performed for both back and front cells, as shown in Figure 4f. After calculation of J_{sc} using EQE spectra, values of 16.1 mA/cm^2 for front cell and 15.95 mA/cm^2 for back cell were obtained, which are very close to each other. This great current density match is originated from the presence of nanostructured ETL in the front cell and employing low bandgap PbS QDs in the back cell. In addition to 2T-tandem devices, we also fabricated 4T-tandem perovskite/PbS QDs devices by fabrication of two separated devices, semi-transparent PSCs and PbS QDs devices. The semi-transparent PSC is consisted of ITO/ZnO/ZnO NWs/SnO_2/Perovskite/CuPC/ITO. In fact, in a 2T tandem device, we just need to get the highest current match for both subcell. However, for the case of 4T tandem devices, we need to achieve the highest PCE for each subcell. Therefore, the optimization process of 2T and 4T tandem cells are different. In order to achieve higher PCE in PSC subcell, we increase the thickness of the perovskite film. After tuning the thickness of perovskite film in the semi-transparent PSC front cell, PCEs of 18.5% and 2.82% for semi-transparent PSC and filtered PbS QDs device were achieved under 1 sun and reverse bias, respectively, as shown in Figure 4g, which results in a 4T-tandem device with PCE of

21.32%. As shown in Table S6, our subcell and tandem devices show a negligible hysteresis effect. We also measured the stabilized PCE of our devices under continuous illumination for 60 s, as shown in Figure 4h. As seen, the 2T-tandem, 4T-tandem, semi-transparent PSC, and filtered PbS QDs devices show stabilized PCEs of 17.1%, 21.1%, 18.3, and 2.8%, respectively. To verify the J_{sc} of both subcells in 4T-tandem devices, EQE spectra of these devices were meausred as shown in Figure 4i. Our calculations indicate J_{sc} of 20.3 mA/cm^2 for semi-transparent PSC (because of using thicker perovskite layer) and 11.2 mA/cm^2 for PbS QDs device.

Stability is one of the main challenges in the PSCs field, which is compulsory step for commercialization of PSCs.[46] Consequently, we measured the stability of our 2T-tandem device at maximum power point, under continuous illumination and nitrogen flow. We first tracked the V_{oc} of this device over 200 s, as shown in Figure 4j. As seen, the V_{oc} is stable over time with a value of over 1.55 V. Figure 4k depicts the operational stability results of this device over 500 h under continuous illumination. From the results, the 2T-tandem device retains 94% of its initial PCE value, which is a great stability for such design. In fact, PbS QDs device has excellent stability in ambient condition (Figure S21), even in humid environment.[30] As can be observed in the inset image of Figure 4k, the contact angle of water droplet on the surface of PbS QDs layer is ~97°, which can effectively protect the PSCs front cell from humidity. Consequently, combining PSCs and PbS QDs solar cells in a tandem device is a great advantage not only to improve the PCE and V_{oc} of the device, but also to enhance the ambient stability of the PSCs. Figure S23 shows the ambient stability results of a single junction PSC and a perovskite/PbS QDs 2T tandem device in a humid environment with 65% RH. As can be observed from the results, the tandem device shows no PCE loss after 72 days in these conditions, whereas the single junction PSC degraded very fast in the

same condition with 37% PCE loss. This result highlights the role of PbS QDs as a great protection layer on ambient stability for the perovskite/PbS QDs tandem design.

Conclusions

In summary, we fabricated perovskite/PbS QDs tandem devices with 2T and 4T configurations and improved the PCE and stability of these solar cells by employing interface engineering and light management techniques. By incorporation of ZnO NWs ETL in the PSCs (front cell in tandem design) and using interface engineering strategy for NWs array using ALD-SnO_2, we achieved a stable and high-performance PSC with a PCE of 22.15%. Moreover, we improved the PV parameters of the PbS QDs device (as back cell in tandem design) by surface passivation of QDs using $CdCl_2$. Using this modification, a PbS QDs device (bandgap ~0.92 eV) with enhanced PCE of 8.46% was obtained. After proper optimization of the thickness and current match, 2T and 4T tandem perovskite/PbS QDs solar cells with stabilized PCEs of 17.1% and 21.1% were achieved, indicating the potential of both perovskite and PbS QDs active layers for the fabrication of high-performance thin film devices. Beside efficiency, the stability of the 2T tandem device is drastically enhanced compared with a single junction PSC. From the operational stability result, the 2T-tandem device showed only 6% PCE loss after 500 h under illumination. More importantly, under humid condition (65% RH), the 2T tandem device showed impressive air stability by retaining its initial PCE value after 70 days, while the single junction PSC indicated 37% PCE loss in the same condition. This result highlights the role of PbS QDs back cell as a great protection layer for PSCs.

References

1. D.-Y. Son, J.-W. Lee, Y. J. Choi, I.-H. Jang, S. Lee, P. J. Yoo, H. Shin, N. Ahn, M. Choi, D. Kim and N.-G. Park, *Nature Energy*, **2016**, *1*, 16081.

2. Q. Luo, H. Ma, Q. Hou, Y. Li, J. Ren, X. Dai, Z. Yao, Y. Zhou, L. Xiang, H. Du, H. He, N. Wang, K. Jiang, H. Lin, H. Zhang and Z. Guo, *Adv. Funct. Mater.*, **2018**, *28*, 1706777.

3. M. M. Tavakoli, W. Tress, J. V. Milić, D. Kubicki, L. Emsley and M. Grätzel, *Energy Environ. Sci.*, **2018**, *11*, 3310–3320.

4. C. Eames, J. M. Frost, P. R. F. Barnes, B. C. O'Regan, A. Walsh and M. S. Islam, *Nat. Commun.*, **2015**, *6*, 7497.

5. Z. Li, R. Wang, J. Xue, X. Xing, C. Yu, T. Huang, J. Chu, K. L. Wang, C. Dong, Z. Wei, Y. Zhao, *JACS*, **2019**, *141*, 17610-17616.

6. M. M. Tavakoli, M. Saliba, P. Yadav, P. Holzhey, A. Hagfeldt, S. M. Zakeeruddin and M. Grätzel, *Adv. Energy Mater.*, **2019**, *9*, 1802646.

7. G. Grancini, C. Roldán-Carmona, I. Zimmermann, E. Mosconi, X. Lee, D. Martineau, S. Narbey, F. Oswald, F. De Angelis, M. Graetzel and M. K. Nazeeruddin, *Nat. Commun.*, **2017**, *8*, 15684.

8. M. M. Tavakoli, S. M. Zakeeruddin, M. Grätzel, Z. Fan, *Adv. Mater.* **2018**, *30*, 1705998.

9. W. Liu, L. Chu, N. Liu, Y. Cheng, F. Wu, Y. Li, Y. Pu, J. Zhang, X. A. Li, W. Huang, *Adv. Mater. Interfaces*, **2019**, *6*, 1801976.

10. M. M. Tavakoli, F. Giordano, S. M. Zakeeruddin and M. Grätzel, *Nano Lett.*, **2018**, *18*, 2428–2434.

11. National Center for Photovoltaics (NCPV) at the National Renewable Energy Laboratory (NREL), www.nrel.gov/pv/assets/images/efficiency-chart.png (accessed: March 2020).

12. M. M. Tavakoli, P. Yadav, R. Tavakoli and J. Kong, *Adv. Energy Mater.*, **2018**, *8*, 1800794.

13. N. J. Jeon, H. Na, E. H. Jung, T. Y. Yang, Y. G. Lee, G. Kim, H. W. Shin, S. Seok, J. Lee and J. Seo, *Nat. Energy*, **2018**, *3*, 1–8.

14. P. Yadav, S. H. Turren-Cruz, D. Prochowicz, M. M. Tavakoli, K. Pandey, S. M. Zakeeruddin, M. Grätzel, A. Hagfeldt, M. Saliba, *J. Phys. Chem. C*, **2018**, *122*,15149-15154.

15. M. M. Tavakoli, P. Yadav, D. Prochowicz, M. Sponseller, A. Osherov, V. Bulović and J. Kong, *Adv. Energy Mater.*, **2019**, *9*, 1803587.

16. S. F. Leung, Q. Zhang, M. M. Tavakoli, J. He, X. Mo, Z. Fan, *Small*, **2016**, *12*, 2536-2548.

17. C. T. Zuo and L. M. Ding, *Nanoscale*, **2014**, *6*, 9935–9938.
18. X. Zheng, B. Chen, J. Dai, Y. Fang, Y. Bai, Y. Lin, H. Wei, X. C. Zeng and J. Huang, *Nat. Energy*, **2017**, *2*, 17102.
19. E. H. Jung, N. J. Jeon, E. Y. Park, C. S. Moon, T. J. Shin, T. Y. Yang, J. H. Noh and J. Seo, *Nature*, **2019**, *567*, 511.
20. M. M. Tavakoli, R. Tavakoli, P. Yadav and J. Kong, *J. Mater. Chem. A*, **2019**, *7*, 679–686.
21. Q. Jiang, Y. Zhao, X. Zhang, X. Yang, Y. Chen, Z. Chu, Q. Ye, X. Li, Z. Yin and J. You, *Nat. Photonics*, **2019**, *13*, 460–466.
22. Y. Zhang, M. Gu, N. Li, Y. Xu, X. Ling, Y. Wang, S. Zhou,F. Li, F. Yang, K. Ji, J. Yuan and W. Ma, *J. Mater. Chem. A*, **2018**, *6*, 24693–24701.
23. R. Lin, K. Xiao, Z. Qin, Q. Han, C. Zhang, M. Wei, M. I. Saidaminov, Y. Gao, J. Xu, M. Xiao, A. Li, J. Zhu, E. H. Sargent and H. Tan, *Nat. Energy*, **2019**, *4*, 864–873.
24. J. Xu, C. C. Boyd, Z. J. Yu, A. F. Palmstrom, D. J. Witter, B. W. Larson, R. M. France, J. Werner, S. P. Harvey, E. J. Wolf, W. Weigand, S. Manzoor, M. F. A. M. van Hest, J. J. Berry, J. M. Luther, Z. C. Holman and M. D. McGehee, *Science*, **2020**, *367*, 1097–1104.
25. M. M. Tavakoli, A. Simchi, Z. Fan and H. Aashuri, *Chem. Commun.*, **2016**, *52*, 323–326.
26. Gao, J., Fidler, A. F. & Klimov, V. I. Carrier multiplication detected through transient photocurrent in device-grade films of lead selenide quantum dots. *Nat. Commun.* **2015**, *6*, 8185.
27. Y. Wang, K. Lu, L. Han, Z. Liu, G. Shi, H. Fang, S. Chen, T. Wu, F. Yang, M. Gu, S. Zhou, X. Ling, X. Tang, J. Zheng, M. A. Loi, W. Ma, *Adv. Mater.* **2018**, *30*, 1704871.
28. M. Yuan, M. Liu and E. H. Sargent, *Nat. Energy*, **2016**, *1*, 16016.
29. M. M. Tavakoli, A. Simchi and H. Aashuri, *Mater. Chem. Phys.*, **2015**, *156*, 163–169.
30. M. M. Tavakoli, H. Aashuri, A. Simchi, S. Kalytchuk and Z. Fan, *J. Phys. Chem. C*, **2015**, *119*, 18886–18895.
31. M. A. Hines and G. D. Scholes, *Adv. Mater.*, **2003**, *15*, 1844–1849.
32. H. Choi, J.-H. Ko, Y.-H. Kim and S. Jeong, *J. Am. Chem. Soc.*, **2013**, *135*, 5278–5281.
33. B. Sun, A. Johnston, C. Xu, M. Wei, Z. Huang, Z. Jiang, H. Zhou, Y. Gao, Y. Dong, O. Ouellette, X. Zheng, *Joule*, **2020**, *4*, 1-15.
34. A. Karani, L. Yang, S. Bai, M. H. Futscher, H. J. Snaith, B. Ehrler, N. C. Greenham and D. Di, *ACS Energy Lett.*, **2018**, *3*, 869–874.

35. A. Manekkathodi, B. Chen, J. Kim, S. W. Baek, B. Scheffel, Y. Hou, O. Ouellette, M. I. Saidaminov, O. Voznyy, V. E. Madhavan, A. Belaidi, S. Ashhab and E. Sargent, *J. Mater. Chem. A*, **2019**, *7*, 26020–26028.
36. B. Chen, S. W. Baek, Y. Hou, E. Aydin, M. D. Bastiani, B. Scheffel, A. Proppe, Z. Huang, M. Wei, Y. K. Wang, E. H. Jung, T. G. Allen, E. V. Kerschaver, F. P. García de Arquer, M. I. Saidaminov, S. Hoogland, S. De Wolf, E. H. Sargent, *Nat. Commun.* **2020**, *11*, 1257.
37. M. M. Tavakoli, H. T. Dastjerdi, J. Zhao, K. E. Shulenberger, C. Carbonera, R. Po, A. Cominetti, G. Bianchi, N. D. Klein, M. G. Bawendi, S. Gradecak and J. Kong, *Small*, **2019**, *15*, 1900508.
38. D.-Y. Son, J.-H. Im, H.-S. Kim and N.-G. Park, *J. Phys. Chem. C*, **2014**, *118*, 16567–16573.
39. M. M. Tavakoli, R. Tavakoli, Z. Nourbakhsh, A. Waleed, U. S. Virk and Z. Fan, *Adv. Mater. Interfaces*, **2016**, *3*, 1500790.
40. S. Ozu, Y. Zhang, H. Yasuda, Y. Kitabatake, T. Toyoda, M. Hirata, K. Yoshino, K. Katayama, S. Hayase and R. Wang, *Front. Energy Res.*, **2019**, *7*, 11.
41. Y. Lv, R. Yuan, B. Cai, B. Bahrami, A. H. Chowdhury, C. Yang, Y. Wu, Q. Qiao, S. Liu, W. H. Zhang, *Angew. Chem. Int. Ed.*, **2020**, *59*, 11969-11976.
42. H. Sun, K. Deng, Y. Zhu, M. Liao, J. Xiong, Y. Li, L. Li, *Adv. Mater.* **2018**, *30*, 1801935.
43. M. M. Tavakoli, M. H. Mirfasih, S. Hasanzadeh, H. Aashuri and A. Simchi, Surface passivation of lead sulfide nanocrystals with low electron affinity metals: photoluminescence and photovoltaic performance, *Phys. Chem. Chem. Phys.*, **2016**, *18*, 12086–12092.
44. W. Ke, D. Zhao, C. R. Grice, A. J. Cimaroli, G. Fang, Y. Yan, *J. Mater. Chem. A*, **2015**, *3*, 23888-23894.
45. X. W. Sun, D. W. Zhao, L. Ke, A. K. K. Kyaw, G. Q. Lo, D. L. Kwong, *Appl. Phys. Lett.* **2010**, *97*, 166.
46. M. M. Tavakoli, H. T. Dastjerdi, D. Prochowicz, P. Yadav, R. Tavakoli, M. Saliba, Z. Fan, *J. Mater. Chem. A*, **2019**, *7*, 14753-14760.

Acknowledgements

This work was supported by Iran National Science and Technology Foundation (INSF, grant number: 96016250), Iran National Elites Foundation, and Iran Nanotechnology

Innovation Council. M.M.T would like to acknowledge research laboratory of electronics (RLE) at Massachusetts Institute of Technology. H.T.D. would like to thank Natural Sciences and Engineering Research Council of Canada (NSERC) (Award number: PDF–487850–2016) for their support. D.P. acknowledges the financial support from the HOMING program of the Foundation for Polish Science co-financed by the European Union under the European Regional Development Fund (POIR.04.04.00-00-5EE7/18-00). P. Y. acknowledges the DST SERB (CRG/2018/000714) and DST Nano Mission (DST/NM/NT/2018/174).

Competing interests

The authors declare no competing interests.

Additional information

Supplementary information is available in the website.

Here, we develop monolithic perovskite/PbS QDs tandem solar cells using interface engineering and light management techniques and achieve a device with stabilized efficiency of 17.1% and excellent stability.